HZ HER: STELLAR RADIUS FROM X-RAY ECLIPSE OBSERVATIONS, EVOLUTIONARY STATE, AND A NEW DISTANCE

D. A. Leahy and M. H. Abdallah
Department of Physics, University of Calgary, Calgary, Alberta T2N 1N4, Canada
Received 2014 May 28; accepted 2014 July 28; published 2014 September 9

ABSTRACT

Observations of HZ Her/Her X-1 by the *Rossi X-Ray Timing Explorer* (*RXTE*) covering high state eclipses of the neutron star are analyzed here. Models of the eclipse are used to measure the radius and atmospheric scale height of HZ Her, the stellar companion to the neutron star. The radius is 2.58–3.01 $\times 10^{11}$ cm, depending on system inclination and mass ratio (q), with an accuracy of ∼1 part in 1000 for given inclination and q. We fit Kurucz model stellar atmosphere models to archival optical observations. The resulting effective temperature ($T_{\rm eff}$) of the unheated face of HZ Her is determined to be in the 2σ range of 7720 K–7865 K, and metallicity ($\log(Z/Z_\odot)$) in the range of -0.27 to $+.03$. The model atmosphere surface flux and new radius yield a new distance to HZ Her/Her X-1, depending on system inclination and q: a best-fit value of 6.1 kpc with upper and lower limits of 5.7 kpc and 7.0 kpc. We calculate stellar evolution models for the range of allowed masses (from orbital parameters) and allowed metallicities (from optical spectrum fits). The stellar models agree with $T_{\rm eff}$ and the radius of HZ Her for two narrow ranges of mass: 2.15–2.20 $M_\odot$ and 2.35–2.45 $M_\odot$. This lower mass range implies a low neutron star mass (1.3 $M_\odot$), whereas the higher mass range implies a high neutron star mass (1.5–1.7 $M_\odot$).

Key words: binaries: eclipsing – stars: individual (HZ Her/Her X-1) – stars: neutron

Online-only material: color figures

1. INTRODUCTION

Her X-1/HZ Her is a bright and well-studied persistent X-ray binary pulsar (e.g., Klochkov et al. 2009; Ji et al. 2009; Leahy 2002, 2003; Igna 2010; Crosa & Boynton 1980; Gerend & Boynton 1976). The system is located at a distance of approximately 6 kpc from Earth. It consists of an A7-type stellar companion (HZ Her), which varies between late A and early B with the orbital phase, and a neutron star (Her X-1) with masses of ∼2.2 $M_\odot$ and ∼1.5 $M_\odot$, respectively (Reynolds et al. 1997). An updated set of binary parameters is given by Staubert et al. (2009). It is one of the few neutron star binaries to have low interstellar absorption, which makes it feasible for observation and study at various wavelengths (e.g., Leahy 2002, 2003; Scott et al. 2000; Scott & Leahy 1999). It is additionally of special interest because it is the neutron star with the best-known mass-to-radius ratio (Leahy 2004b). This value was made possible by a definitive determination of the geometry of the emitting region on the neutron star from a study of the 35 day evolution of the pulse profile (Scott et al. 2000). Thus, it of great interest to constrain the mass of the neutron star better than the current range of $\simeq 1.3$–1.5 $M_\odot$. This would allow the determination of both mass and radius with tight constraints and form a strong constraint on equations of state for dense matter in neutron stars.

Emission from Her X-1/HZ Her covers the optical, ultraviolet, EUV, and X-ray regime and models for the, often coupled, emission processes must ultimately be consistent. X-ray spectra of Her X-1 are discussed by Oosterbroek et al. (1998) and Dal Fiume et al. (1998; from *BeppoSAX*), Choi et al. (1997; from *ASCA*) and Leahy (1995b; from *GINGA*). The hard X-rays (>1 keV) arise as a result of mass accretion onto the neutron star and are modulated by the neutron star rotation and obscuration by the accretion disk (e.g., Scott et al. 2000 and references therein), companion star and cold gas in the system that causes the absorption dips (Leahy 1997; Igna & Leahy 2011, 2012). A small reflected/reprocessed X-ray component

is present that is observable during the low state and eclipses (Choi et al. 1994; Leahy et al. 1995a). A major portion of the observed optical/ultraviolet emission is believed to arise from X-ray heating of HZ Her and the accretion disk. The X-ray heating causes the surface temperature of HZ Her facing the neutron star to be approximately 10,000 deg higher than the cooler shadowed side (Cheng et al. 1995). Analysis of ultraviolet spectra of Her X-1 are presented by Boroson et al. (1997) and Vrtilek & Cheng (1996). Optical signatures of reprocessing on the companion and accretion disk are discussed by Still et al. (1997). Observations of the broadband optical emission of HZ Her/Her X-1 have been presented by Deeter et al. (1976) and Voloshina et al. (1990), among others. Between the hard X-ray and optical/ultraviolet band lies the soft X-ray/extreme ultraviolet band (∼0.016–1 keV). A blackbody spectral component has been detected by many previous observations with a temperature of about 0.1 keV (e.g., Shulman et al. 1975; Oosterbroek et al. 2000) and generally has been attributed to the reprocessing of hard X-rays in the inner region of the accretion disk (e.g., McCray et al. 1982; Oosterbroek et al. 2000).

Her X-1 shows a variety of phenomena at different timescales, including 1.24 s pulsations, orbital eclipses with a period of 1.7 days and a 35 day cycle in the X-ray flux. The latter normally consists of a bright state, known as the Main High state, which lasts 10–12 days and an intermediate-brightness state, the Short High state, which lasts 5–7 days. These two states are separated by 8–10 day long low states. The precessing accretion disk causes the alternating pattern of High and Low X-ray intensity states by periodically blocking the neutron star from view. The initial rapid flux rise over a few hours marks the start of a High state and is known as the "turn-on." This event is the emergence of the neutron star from behind the moving outer disk edge (see Scott et al. (2000) and references therein). Discussions of the properties of the 35 day cycle are given by Leahy & Igna (2010), Scott & Leahy (1999), and Shakura et al. (1998). The X-ray pulse profile evolution has been

Table 1
RXTE/PCA Main High Eclipse Observations[a]

Type[b]	MJD	ϕ_{35}[c]	$\phi_{orb,start}$	$\phi_{orb,end}$
E	50357	0.027	.0617	.0746
E	50360	0.127	.0617	.0799
I	50361	0.169	.9200	.9337
I	50710	0.176	.9201	.9319
E	52597	0.081	.0645	.0776
I	52599	0.122	.9200	.9340
E	52599	0.129	.0670	.0799
I	52601	0.170	.9200	.9406

Notes.
[a] Start and end of continuous observations of each eclipse given.
[b] I for ingress, E for egress.
[c] ϕ_{35} is 35 day cycle phase.

convincingly linked to the precessing accretion disk by Scott et al. (2000). Over the course of the 35 day cycle, the broadband optical emission exhibits a complex, systematic variation, in addition to the orbital modulation due to X-ray heating of HZ Her. This pattern is a consequence of disk emission and of disk shadowing/occultation of the heated face of HZ Her by the precessing accretion disk (Gerend & Boynton 1976).

The regular variability in Her X-1 that is of interest here is the X-ray eclipse of the neutron star during Main High. During Main High, the observer has a direct view of the neutron star, thus that eclipse probes the structure of the companion star HZ Her. The previous study of this nature was carried out by Leahy & Yoshida (1995) using one eclipse observed with *GINGA*. Here we consider all Main High eclipses from the *Rossi X-Ray Timing Explorer*/Proportional Counter Array (*RXTE*/PCA) data archive, covering more than one decade of observations of Her X-1. Accurate measurements of the radius of HZ Her are made and combined with constraints from optical spectra of HZ Her during eclipse, which yield effective temperature (T_{eff}) and metallicity (Z), to obtain a new distance to the system. We compare the observationally determined radius and effective temperature to stellar evolution calculations to determine allowed masses for HZ Her, then use those to explore the allowed parameters of the system, including the mass of the neutron star.

2. *RXTE* OBSERVATIONS OF ECLIPSES AND ANALYSIS

2.1. Eclipse Light Curves

A summary analysis of the entire *RXTE*/PCA set of Standard 2 data is given in Leahy & Igna (2011). Here, we are interested in analyzing Main High ingresses or egresses to obtain values of the radius of HZ Her. These eclipses are known to occur rapidly (over a few minutes) at orbital phases $\simeq 0.93$ and $\simeq 0.07$ (e.g., Leahy & Yoshida 1995) and are caused by the limb of HZ Her covering the observer's line of sight to the neutron star. The part of the data that occurs during Main High state was determined here using the Main High turn-on times of Leahy & Igna (2010). The Main High data was, in turn, searched for all data during orbital phases of eclipse (including ingress and egress: phase 0.92–1.08). Nineteen different eclipses were observed with varying amounts of phase coverage. Counting the ingress part (phase 0.92–1.0) and egress part (phase 0.0–0.08) separately, there were 23 ingresses or egresses during Main High state. Some of these were observed with too little phase coverage to measure the ingress or egress light curve. Several

Table 2
HZ Her/Her X-1 Orbital Parameters

Parameter	Value(uncertainty)	Reference[a]
P_{orb}	1.700167590(2)d	(1)
$\dot{P}_{orb}$	$4.85(13) \times 10^{-11}$ s/s	(1)
$T_{\pi/2}$	MJD46359.871940(6)	(1)
$a_x \sin(i)$	13.1831(4) lt-s	(1)
Eccentricity	$4.2(8) \times 10^{-4}$	(1)
f_M	$0.85059(8)\ M_{\odot}$	(3)
K_c	109(10) km s^{-1}	(2)

Note. [a] (1) Staubert et al. (2009); (2) Reynolds et al. (1997); (3) calculated here.

Table 3
Semi-major Axis[a] and Masses of HZ Her (M_c) and Her X-1 (M_x)

K_c(km s^{-1})	99			109			119		
q	0.5856			0.6448			0.7039		
Inclination	a	M_c	M_x	a	M_c	M_x	a	M_c	M_x
80°	6.364	2.239	1.311	6.601	2.409	1.553	6.838	2.586	1.820
82°.5	6.321	2.194	1.354	6.557	2.361	1.522	6.793	2.534	1.784
85°	6.291	2.163	1.335	6.525	2.328	1.501	6.760	2.498	1.758
87°.5	6.273	2.145	1.323	6.507	2.308	1.488	6.741	2.477	1.743
90°	6.267	2.139	1.319	6.501	2.301	1.484	6.734	2.470	1.738

Note. [a] Semi-major axis, a, is in units of 10^{11} cm, masses are in $M_{\odot}$.

other ingresses or egresses include cold matter absorption immediately around the time of ingress or egress. This is seen from the low (2–4 keV)/(9–20 keV) softness ratio coinciding with below-normal count rates, which indicates absorption. Sporadic absorption events (dips) are regularly seen during the Main High state. This has been recently quantified by Leahy & Igna (2011): their Figure 5 shows the data for the Main High state folded on the orbital period, with absorption dips seen as drops in count rate simultaneous with a decrease in the (2–4 keV)/(9–20 keV) softness ratio; their Figure 7 shows the fraction of time spent in dips to the total time observed as a function of orbital phase in Main High state. Around the time of eclipse, this fraction is between 0.3 and 0.6. There were four clear (without excess absorption) ingresses and four clear egresses suitable for analysis. Figure 1 shows the *RXTE* (9–20 keV) light curves for these eight ingresses/egresses and Table 1 gives the MJD, 35 day phase and orbital phase coverage of these observations.

2.2. Orbital Parameters of HZ Her/Her X-1

To model the system orbit, we use the most recent published orbital parameters, given by Staubert et al. (2009). These parameters are summarized here in Table 2. To calculate the absolute size of the orbit, the mass ratio is needed, which can be found from the amplitude of the velocity of the companion star HZ Her, K_c, together with the amplitude of the velocity of the neutron star, K_x (from $q = M_x/M_c = K_c/K_x$). Because K_x is already very well known through pulse time delays, a good value for K_c is needed. The best-fit value (Reynolds et al. 1997) is $K_c = 109$ km s^{-1} with a quoted statistical error of 3 km s^{-1} and systematic error of $\sim$10 km s^{-1}. Here, in addition to the best-fit case, we take a low K_c case of 99 km s^{-1} and a high K_c case of 119 km s^{-1} value. A range of inclinations between 80° and 90° was chosen, which is somewhat larger than normally adopted inclinations ($\simeq 83°$–$\simeq 87°$) to explain the 35 day cycle (see, e.g., Leahy 2002). The inclination and K_c values significantly affect the orbit size and the masses of the two components HZ Her and Her X-1, as shown in Table 3; errors in the masses and size of
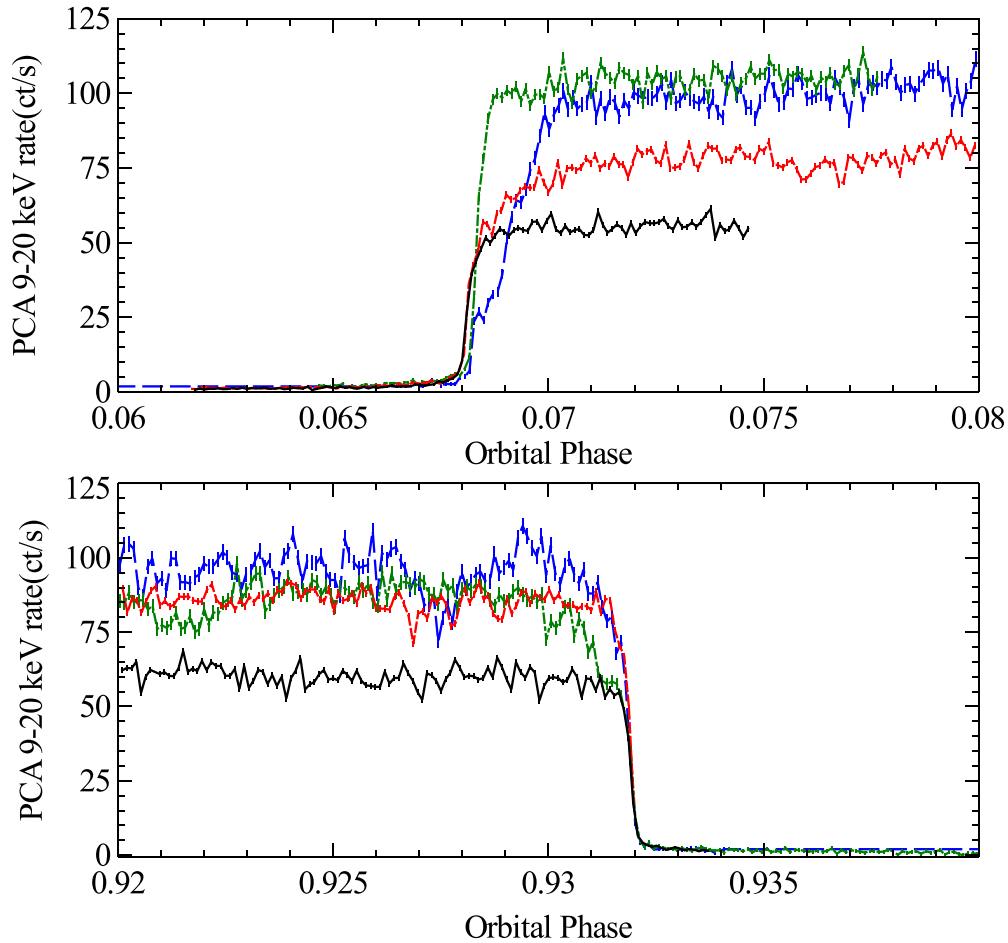
Figure 1. High State eclipses without excess absorption observed with *RXTE*/PCA: the four egresses (top panel: MJD50357—black, solid line; MJD50361—red, dashed line; MJD52597—green, dash-dotted line; MJD52599—blue, long-dashed line) and four ingresses (lower panel: MJD50361—black, solid line; MJD50710—red, dashed line; MJD52599—green, dash-dotted line; MJD52601—blue, long-dashed line).

(A color version of this figure is available in the online journal.)

the orbit have a negligible contribution from the other measured orbital parameters.

2.3. Eclipse Light Curve Model

A numerical model was constructed and fitted to the observed light curves to determine the radius of HZ Her. The duration of eclipse in orbital phase is determined by the amount of angle, relative to 360° of a full rotation of the binary system, during which HZ Her blocks the line of sight to the neutron star. The conversion of this angle into physical size depends on the binary separation, a. The conversion of this size into a stellar radius depends on the binary inclination, i, as the line of sight makes a different cut across the back face of the star depending on inclination.

A few approximations are made in the model used here. The eccentricity of the orbit is very small (see Table 2), enough that use a circular orbit gives accurate results (to one part in 10^4). The atmosphere of the star was taken to have an exponential density profile, and the radius of the star was defined as the radius where the vertical optical depth was unity in the 9–20 keV X-ray band. For the 9–20 keV band, the absorption plus scattering opacity was taken to be sum of the photoelectric and Thompson cross-sections, using the matter of solar composition. The neutron star is taken as a point source of X-rays. The accretion column that emits the bulk of the X-rays is small enough (<a few km; Leahy 2004a, 2004b) that a point source is a good assumption for the

X-ray source. A few km is small compared to the next smallest scale involved, which is the scale height of the atmosphere of HZ Her ($\sim 6 \times 10^8$ cm; Leahy & Yoshida 1995). HZ Her is essentially Roche-lobe filling (e.g., Leahy & Scott 1998), thus it is not spherical but has the shape of the Roche lobe.

The model initially uses a spherical star and yields the impact parameter from the center of the star to the line of sight through the stellar surface at vertical optical depth unity. We call this distance $R_{tan}(\tau = 1)$ (or for simplicity, just R_{tan}). Knowing the shape of the Roche lobe, which depends only on q, we use R_{tan} to calculate the distance to any other part of the surface on the Roche lobe.

We fit the model to each of the eight observed ingresses and egresses. The MJD52599 egress (Figure 1 top panel) shows an extended slow rise after orbital phase 0.068: the fit for this egress was restricted to the early sharp rising part of the egress. For the MJD52599 ingress (Figure 1 bottom panel) there is a shallow decrease prior to the main sharp ingress—the fit was restricted to the sharp part of the ingress. The eight ingresses/egresses were fit separately in order to demonstrate that a single radius can explain all events, so that there is no evidence that the radius of HZ Her is time-variable. The resulting radii (R_{tan}) and scale heights (H) are given in Table 4 for the case of 85° inclination and $K_c = 109$ km s^{-1}. The uncertainty of R_{tan} is $\sim 10^8$ cm and of H is $\sim 10^8$ cm (i.e., similar in absolute magnitude, but the relative uncertainty in R_{tan} is three orders of magnitude smaller).

Table 4
Radii from X-Ray Eclipse Models for $85°$ Inclination, $K_c = 109$ km s^{-1}

Type[a]	MJD	$R_{\tan}(\tau = 1)$[b] (cm)	H[c] (cm)
E	50357	2.735×10^{11}	5×10^8
E	50360	2.734×10^{11}	5×10^8
I	50361	2.736×10^{11}	5×10^8
I	50710	2.735×10^{11}	5×10^8
E	52597	2.742×10^{11}	5×10^8
I	52599	2.736×10^{11}	5×10^8
E	52599	2.741×10^{11}	5×10^8
I	52601	2.734×10^{11}	5×10^8

Notes.
[a] I for ingress, E for egress.
[b] $R_{\tan}(\tau = 1)$ is the radius derived assuming a spherical star; see the text.
[c] H is the scale height of an exponential atmosphere.

Table 5
Radii, $R_{\tan}(\tau = 1)$[a], Averaged over Eclipses at Each Inclination

Inclination	$K_c = 99$ km s^{-1}	$K_c = 109$ km s^{-1}	$K_c = 119$ km s^{-1}
$80°$	2.805	2.910	3.015
$82°.5$	2.709	2.810	2.911
$85°$	2.638	2.737	2.835
$87°.5$	2.596	2.692	2.789
$90°$	2.581	2.677	2.774

Notes. [a] $R_{\tan}(\tau = 1)$ is given in units of 10^{11} cm. To obtain the equivalent radius, R_L, of a Roche-lobe filling star with the same volume, multiply by a factor that depends on mass ratio and inclination (see the text for details).

We find that for a given inclination and K_c, all eight eclipses give the same $R_{\tan}$ within errors. This confirms that we are measuring the radius of HZ Her and not some other variable phenomenon, e.g., one related to the accretion disk or stream. As a result, we average $R_{\tan}$ over the eight eclipses for each inclination and K_c and present the results in Table 5.

For all of the eclipses, inclinations and K_c values, H is consistent with a constant value of 5×10^8 cm, consistent with the value found by Leahy & Yoshida (1995). The uncertainty in $R_{\tan}$ here is estimated from the root mean square of the eight best-fit values of $R_{\tan}$ for each inclination at K_c value, which ranges from $.0023 \times 10^{11}$ to $.0031 \times 10^{11}$ cm for the fifteen different cases.

Next, we calculate a correction for the non-spherical shape of the surface of the star, which is filling its Roche lobe, using the standard Roche potential. The radius derived for a spherical star, $R_{\tan}$ (listed in Table 5), is from the center of HZ Her, to the point on the Roche lobe surface tangent to the line of sight from the observer to the neutron star. We will need the cross-sectional area of the star viewed by the observer: this will be used in Section 4.1 together with the surface flux to derive the distance to the binary. For the fifteen different cases (five inclinations and three mass ratios—see Table 3) $R_{\tan}$ ranged from 0.412 to 0.441 times the orbital separation. To determine the cross-sectional area of the star at mid-eclipse, because the system inclination is near $90°$, we can use the area of an ellipse with major-axis radius $R_{\tan}$, and the minor axis of the polar radius of HZ Her's Roche lobe. We find that the polar radius ranges from 0.943 to 0.948 times $R_{\tan}$. Thus, to an accuracy of about one part in 400, we use a fixed ratio of 0.9455 for all cases, which gives a cross-sectional area during eclipse of $0.9455\pi R_{\tan}^2$.

For comparison with stellar models, one needs the radius of a sphere, R_L, with the same volume as the distorted star. In the case of HZ Her, the star just fills its Roche lobe, thus we can use the formula of Eggleton (1983), which relates R_L/a to mass ratio, q. For the three different cases of mass ratio here (see Table 3) one obtains $R_L/a = 0.426, 0.417$ and 0.410, respectively. To determine the radius of the spherical star of the same volume, the $R_{\tan}$ radii in Table 5 need to be multiplied by the ratio of $R_L/R_{\tan}$, which depends on mass ratio, q, and inclination. For $q = 0.586$, this ratio ranges from 1.0047 ($80°$ inclination) to 1.0025 ($90°$), while for $q = 0.645$, the range is 1.0060 to 1.0041, and for $q = 0.704$, it is 1.0071 to 1.0052. Thus, to one part in 400, this ratio can be taken as 1.005 for all cases here. However, we used the more accurate numerically calculated value of the ratio to obtain R_L for each case of q and inclination separately.

3. CONSTRAINTS ON EFFECTIVE TEMPERATURE AND METALLICITY OF HZ HER

During the eclipse of the neutron star, only the unheated surface of HZ Her is viewed from Earth. The optical spectrum during eclipse has been used to estimate the luminosity, and thus the distance of HZ Her/Her X-1 previously (e.g., Oke 1976; Cheng et al. 1995). Here, we compare moderately high resolution optical observations to the detailed set of stellar atmosphere spectra computed by Kurucz (1993) over a comprehensive grid in $T_{\rm eff}$ and $\log(Z/Z_\odot)$ and with $\log(g)$ set to the value appropriate for HZ Her.

High resolution optical spectra of HZ Her during orbital eclipse were published by Anderson et al. (1994), and were taken with the *Hubble Space Telescope* (*HST*) Faint Object Spectrograph (FOS; for the wavelength ranges of ∼1200–1600 Å and ∼2230–3230 Å) and with the *Kitt Peak National Observatory* GoldCam instrument (for the wavelength ranges ∼3200–6000 Å). However, as noted by Cheng et al. (1995), the GoldCam spectrum is not flux-calibrated, and thus is not suitable for use in quantitative modeling. Earlier spectrophotometry for the wavelength range of ∼3000–10000 Å was published by Oke (1976) for orbital phase 0.011 (hereafter referred to as Oke data): those data have an absolute flux calibration and are suitable for use here. The GoldCam data was directly compared to the Oke data. It is found that the GoldCam data is slightly different in shape, but noticeably higher (15%) in flux—much larger than the data errors. This confirms the lack of flux calibration of the GoldCam data. The *HST*/FOS, GoldCam, and Oke data sets are not simultaneous, but the back side of HZ Her should not be variable.

The *HST*/FOS data covers two wavelength ranges (2220–3200 Å and 1285–1604 Å) and were taken with resolution $(\lambda/\Delta\lambda) \simeq 1300$. The GoldCam data covers the range of 3500 Å–6000 Å, with 3.9 Å resolution. We digitized the *HST*/FOS and GoldCam data at orbital phase 0 from Figures 2(c) and (d) of Anderson et al. (1994) at resolutions of ∼2 Å and 4 Å, respectively. The data errors were estimated from the figures. The short wavelength *HST*/FOS data (1285 Å–1604 Å) from Figure 2(b) of that paper were not used for final analysis because they are dominated by the line emission from hot gas (e.g., Anderson et al. 1994; Cheng et al. 1995) and not HZ Her. The Oke data were digitized and the data errors were estimated from the Table 2 of Oke (1976). Those data (covering 3280–9880 Å) have a bandpass of 40 Å for wavelengths less than 5800 Å and 80 Å for wavelengths greater than 5800 Å, with a
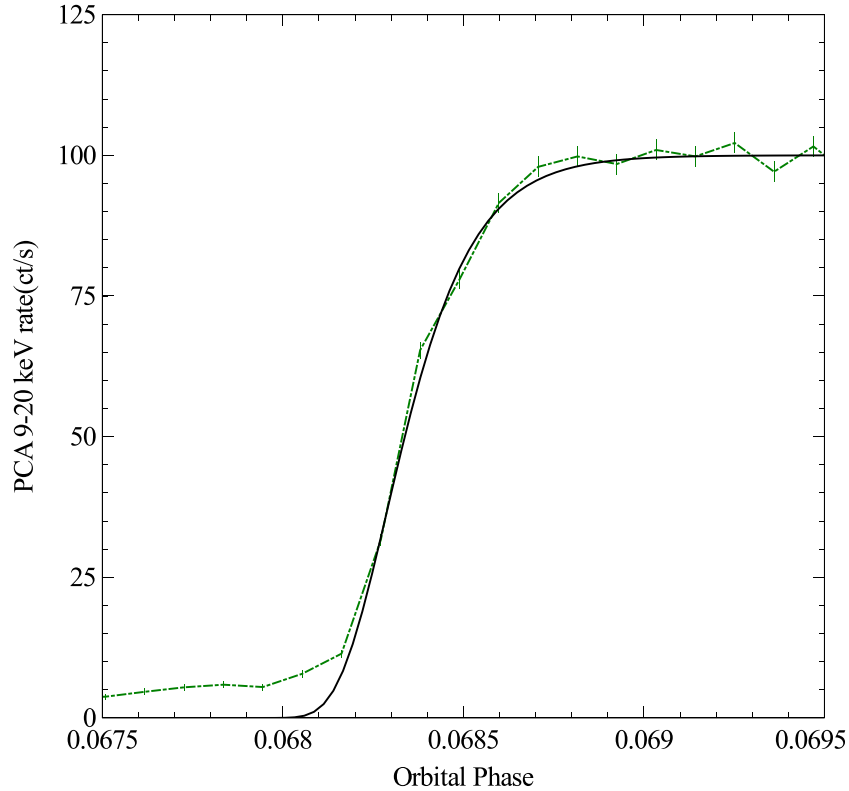
Figure 2. Model (black, solid line) and observed light curve for the eclipse egress on MJD52597 (green, dash-dotted line). See the text for a description of the model. (A color version of this figure is available in the online journal.)

few wavelength bins missing. The combined data set used here for analysis consisted of the Oke data plus the *HST*/FOS 2220 to 3200 Å data.

The Kurucz stellar atmosphere models are available as fits files from the Space Telescope Science Institute (STScI) Web site. They have spectral resolutions (bin sizes) of 10 Å over the range of 1200–3000 Å and 20 Å above 3000 Å. Prior to carrying out any spectral fits, the *HST*/FOS data were rebinned to match the bins for the lower-resolution Kurucz model atmospheres in the range of 2220–3200 Å. The Kurucz model atmosphere data were rebinned to match the bins for lower-resolution Oke data in the range of 3280–9880 Å. This resulted in 183 wavelength bins for the observations and the matching Kurucz models. Fitting was based on least-squares (χ^2) minimization. To be conservative and to allow for some systematic errors, the estimated errors of the *HST*/FOS and Oke data sets were multiplied by a factor of 1.8. This does not affect the best fits but makes the 2σ and 3σ limits on $T_{\rm eff}$ and $\log(Z/Z_\odot)$ obtained from the spectral fits somewhat larger (about a factor of two) than if no allowance is made for an additional source of error.

The resulting allowed mass range of HZ Her is $\simeq 2.2$–$2.5\,M_\odot$ (see Table 3) with higher values for lower inclinations. The stellar radius from the eclipse fits gives higher values for lower inclinations, resulting in a calculated surface gravity of $\log(g)$ nearly equal 3.50 for all inclinations. Thus, we fixed $\log(g) = 3.50$ for all stellar atmosphere models, leaving $T_{\rm eff}$ and $\log(Z/Z_\odot)$ as free parameters.

We carried out fits of stellar atmosphere spectra for a wide range of $T_{\rm eff}$ and $\log(Z/Z_\odot)$. The results are presented in Table 6. The minimum χ^2 per degree of freedom (182, since these fits have one free parameter normalization) is $\simeq 1$, indicating that our error estimates are reasonable. These fit showed that $T_{\rm eff}$

Table 6
χ^2 for Fits[a] to the HZ Her Near UV–Optical Spectrum

$T_{\rm eff}$	7700 K	7750 K	7800 K	7850 K	7900 K
$\log(Z/Z_\odot)$					
−0.3	222.5	220.4	225.9	241.4	264.8
−0.2	221.0	213.9	214.2	224.7	244.1
−0.1	229.0	217.0	211.1	215.7	230.2
0.0	247.8	229.9	216.7	215.1	223.8
+0.1	278.1	254.0	233.0	224.7	226.9

Note. [a] Number of degrees of freedom is 182.

was near the center of the range 7250–8250 K, and indicated that a much better constraint on $T_{\rm eff}$ was achievable. We obtain a new approximate constraint on metallicity, which is refined below: $\log(Z/Z_\odot)$ is in the range −1.0 to +0.2. Outside of the range, the observed spectrum strongly disagrees with the short-wavelength observations and the strength of the Balmer jump at ∼3800 Å.

Next, we carried out fits with a finer grid of stellar models with $T_{\rm eff}$ in the range of 7500 K–8000 K and $\log(Z/Z_\odot)$ in the range of −0.5 to +0.2. To obtain a finer resolution in $T_{\rm eff}$ than the archived spectra from STScI (which was 250 K in $T_{\rm eff}$), we interpolated in the Kurucz models in $T_{\rm eff}$. The result of these spectral fits are summarized in Table 6. The 2σ and 3σ limits for two parameters of interest ($T_{\rm eff}$ and $\log(Z/Z_\odot)$) are $\delta\chi^2 = 6.8$ and 11.8, respectively. We fit with a finer grid of models around the best-fit model to find the allowed region in the $T_{\rm eff}$ versus $\log(Z/Z_\odot)$ plane. The limits of this region are given in Table 7. The extreme edges of the 2σ allowed region extend to 7720 K $< T_{\rm eff} <$ 7865 K and −0.27 $< \log(Z/Z_\odot <$ 0.03. The best-fit model and the observations are shown in Figure 3.
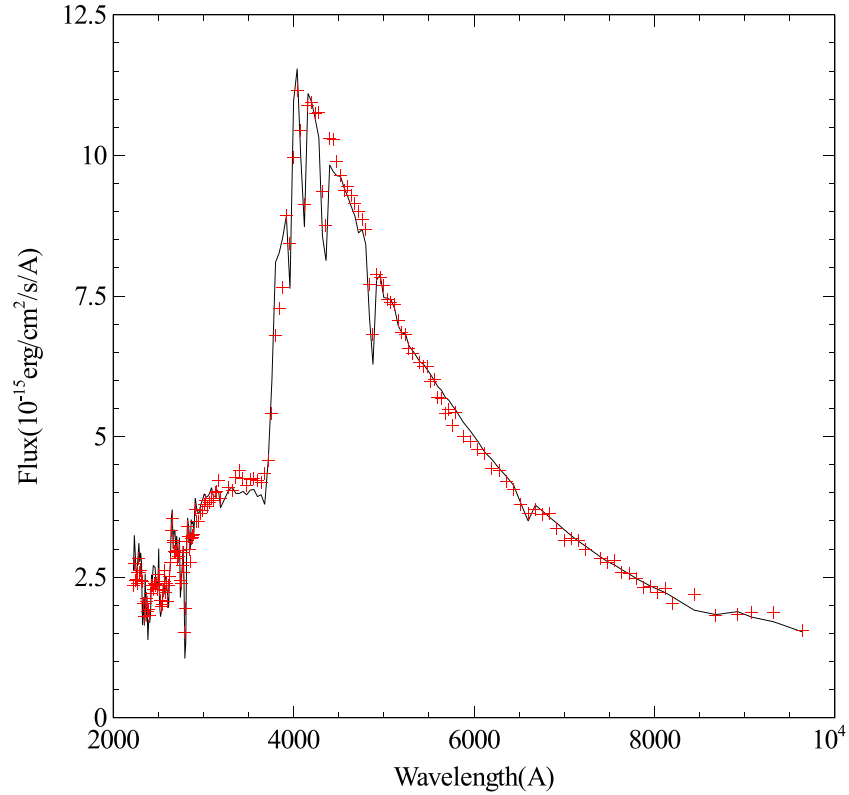
Figure 3. HZ Her observed spectrum during neutron star eclipse, at orbital phase 0 (red points), and best-fit Kurucz model atmosphere spectrum (black line) with $T_{eff} = 7800$ K, $\log(Z/Z_\odot) = -0.1$, and $\log(g) = 3.5$.

(A color version of this figure is available in the online journal.)

Table 7
2σ and 3σ Limits to T_{eff} and $\log(Z/Z_\odot)$

	Lower Limit 3σ	Lower Limit 2σ	Best-fit	Upper Limit 2σ	Upper Limit 3σ
T_{eff}	7690 K	7720 K	7794 K	7865 K	7895 K
$\log(Z/Z_\odot)$	-0.33	-0.27	-0.12	$+0.03$	$+0.09$

Table 8
Distance[a] and 2σ Upper and Lower Limits versus Inclination and K_c

Inclination	$80°$	$82°.5$	$85°$	$87°.5$	$90°$
$K_c = 99$ km s^{-1}					
Best-fit	6.38	6.16	6.00	5.91	5.87
Lower limit	6.23	6.02	5.86	5.78	5.73
Upper limit	6.50	6.27	6.11	6.02	5.98
$K_c = 109$ km s^{-1}					
Best-fit	6.62	6.39	6.22	6.12	6.09
Lower limit	6.46	6.24	6.08	5.98	5.95
Upper limit	6.74	6.51	6.34	6.24	6.20
$K_c = 119$ km s^{-1}					
Best-fit	6.85	6.62	6.45	6.34	6.31
Lower limit	6.70	6.47	6.30	6.20	6.16
Upper limit	6.98	6.74	6.57	6.46	6.43

Note. [a] Distances are given in units of kpc.

4. DISCUSSION

4.1. A New Distance to HZ Her

We can directly calculate a new distance to HZ Her. The radius of HZ Her is determined from the X-ray eclipses, and the surface flux is determined from the stellar atmosphere model fits to HZ Her. The observed continuum surface flux during eclipse was found by Still et al. (1997) and is shown in Figure 2 (top panel) of that paper, obtained from the line-free wavelength ranges 4745–4755 Å, 4775–4796 Å, and 4898–4912 Å. During mid-eclipse the flux is 6.5 mJy, with an error of $\sim$0.2–0.3 mJy. The Kurucz model atmosphere spectra have 20 Å bins in this wavelength region, thus we chose only line-free bin 4780–4800 Å in the model spectra to obtain the model surface continuum flux. The error in distance caused by the uncertainty in continuum flux is $\sim$2%, small compared to the uncertainties in distance from other factors (inclination and T_{eff}).

We include in the distance calculation the correction for the shape of the Roche lobe, as described above. The resulting distances are given in Table 8. The distances are the best-fit values and the larger (smaller) of the two upper (lower) limits to distance from the 2σ T_{eff} and $\log(Z/Z_\odot)$ limits determined

above. Because the measured stellar radius, R_{tan}, from the X-ray eclipses depends on inclination, the best-fit distance and upper and lower limits depend on inclination.

Our results are about 5% smaller than the distance derived by Reynolds et al. (1997), which is mainly attributed to our T_{eff} of $\simeq$7800 K, which is lower than the value of $\simeq$8100 K they used from Cheng et al. (1995).

4.2. Stellar Models, Mass, and Evolutionary State of HZ Her

Stellar evolution models were obtained using the EZ-Web interface[1] to obtain a basic understanding of the evolutionary

---

[1] The interface can be found at http://www.astro.wisc.edu/~townsend/.

state of HZ Her. The code itself is an updated version of the Eggleton (1971) code, which includes several improvements including the ability to evolve past the Helium flash in low-mass stars. In this simplified treatment, we do not take into account effects of the binary on the stellar evolution, even though there is evidence of mass transfer from the progenitor of Her X-1 onto HZ Her from the enhanced N abundance of HZ Her (Jimenez-Garate et al. 2005). A detailed study of stellar evolution is beyond the scope of this paper. Even so, the available standard stellar evolutionary models in the mass range of interest (2–$2.5\ M_\odot$) are sufficiently reliable to infer the properties of HZ Her.

The mass range of interest is 2.139–$2.586\ M_\odot$ (see Table 3) for an inclination range of $80°$–$90°$. The metallicity ranges of interest are the best fit and upper and lower 2σ limits, given in Table 7. Using $Z_\odot = 0.02$, the best fit and upper and lower limits on Z are 0.015, 0.011, and 0.021, respectively. Models with $Z = 0.01$ and 0.02 were computed to beyond the point where they begin ascent up the giant branch, which happens from ~ 600 Myr to 1 Gyr after the zero-age main sequence, depending on initial mass. The examples plotted here are for $Z = Z_\odot = 0.02$. The evolutionary tracks for stars of 2.2, 2.3, 2.4, and $2.5\ M_\odot$ are shown in Figure 4 for the region of interest here: from zero-age main sequence until they become too cool to possibly represent the current stage of HZ Her, which has $T_{\rm eff} \simeq 7800$ K.

We next compare the evolutionary tracks with the limits on effective temperature, $T_{\rm eff}$, and stellar radius, R. The $T_{\rm eff}$ limits come from the spectral fits to the optical spectrum of HZ Her (discussed above) and are independent of mass of the star. To show the allowed region for HZ Her in the HR diagram, the 2σ upper and lower limits to $T_{\rm eff}$ are shown in Figure 4 by the vertical dotted lines. The values of R derived from the X-ray eclipses depend both on inclination and K_c (see Table 5). However, one can take the global upper and lower limits of R from Table 5 to calculate global upper and lower limits to the luminosity of HZ Her using $L = 4\pi R^2 \sigma_{SB} T_{\rm eff}^4$ with σ_{SB} the Stefan–Boltzmann constant. These temperature-dependent upper and lower limits are plotted on Figure 4 as the sloping dotted lines.

The measured stellar radius, R, has negligible uncertainty other than that from the uncertainty in inclination and K_c. We note that each different evolutionary track is essentially a constant mass track because the mass-loss rates are very small prior to ascending the giant branch. The result is that, with fixed mass for each evolutionary track, K_c and inclination are no longer independent variables. We can take K_c to be a function of inclination. Thus, in order to obtain R limits for each mass, we allow the inclination to vary over its full range ($80°$–$90°$), but reject cases that have K_c outside its allowed range of 99–119 km s^{-1}. A separate calculation is done for each input value of companion mass, M_c. Table 9 gives the allowed range of inclinations and associated K_c for a set of fixed masses for HZ Her. Note that the range of allowed inclination (or K_c) is very small near the mass limits (e.g., for 2.15 and $2.55\ M_\odot$). Also given are the semi-major axis, a, the neutron star mass, M_x, and the eclipse derived radius. The radius at the minimum inclination is larger than that for the maximum inclination, which happens because the line of sight from observer to neutron star makes a cut across the stellar surface at higher latitude at lower inclination. From Table 9, it is seen that the upper and lower limits to stellar radius, R, are significantly different for different masses of HZ Her.

Table 9
Inclination Range and Parameters as a Function of Mass of HZ Her

M_c	2.15	2.2	2.3	2.4	2.5	2.55
Minimum						
$i_{\rm min}$	$86°\!74$	$82°\!11$	$80°$	$80°$	$80°$	$80°$
$K_{c,{\rm min}}$	99.0	99.0	102.6	108.5	114.2	117.0
$a_{\rm min}$	6.279	6.327	6.450	6.588	6.724	6.791
$M_{x,{\rm min}}$	1.260	1.289	1.396	1.540	1.689	1.765
$R(i_{\rm min})$	2.605	2.718	2.843	2.904	2.964	2.971
Maximum						
$i_{\rm max}$	$90°$	$90°$	$90°$	$90°$	$84°\!82$	$81°\!63$
$K_{c,{\rm max}}$	99.7	102.8	108.9	114.9	119.0	119.0
$a_{\rm max}$	6.284	6.356	6.499	6.639	6.776	6.843
$M_{x,{\rm max}}$	1.268	1.338	1.482	1.631	1.786	1.865
$R(i_{\rm max})$	2.582	2.618	2.677	2.734	2.839	2.943

Note. [a] Semi-major axis, a, and radius, R, are in units of 10^{11} cm, masses are in $M_\odot$, and K_c are in units of km s^{-1}.

The net result is that each evolutionary track has it own R limits and (common) $T_{\rm eff}$ limits. Figure 5 shows example evolutionary tracks in the R versus $T_{\rm eff}$ plane for $M = 2.22$ and $2.25\ M_\odot$ and the R limits and $T_{\rm eff}$ limits for these two cases. As time increases the tracks move up and to the left in the diagram, then turn to move down and to the right (a brief time of increasing temperature and decreasing radius), and then move upward and left as the star becomes a red giant. For both 2.22 and $2.25\ M_\odot$ cases, the evolutionary tracks cross their respective allowed regions only during the short phase of increasing temperature and decreasing radius just prior to central hydrogen exhaustion.

We explore a range of masses. Below $2.15\ M_\odot$, the evolutionary track does not pass into the allowed R–$T_{\rm eff}$ region, but below and left of it. Between 2.15 and $2.20\ M_\odot$, the point of central hydrogen exhaustion is inside the allowed region, and the duration that the evolutionary track is in the allowed region is short (~ 100 kyr). Between 2.20 and $2.35\ M_\odot$, the situation is like that for 2.22 and $2.25\ M_\odot$ cases, where the evolutionary track only crosses the allowed region during the phase of increasing temperature and decreasing radius. Between 2.35 and $2.45\ M_\odot$, the evolutionary track crosses the allowed region before the rightward excursion in the R versus $T_{\rm eff}$ diagram, with decreasing temperature and increasing radius (before the leftward turn in the H-R diagram, see Figure 4). Masses above $2.45\ M_\odot$ do not cross the allowed region in the R versus $T_{\rm eff}$ diagram: all three parts of the evolutionary track pass above (too large R) and to the right (too large $T_{\rm eff}$) of the allowed region.

The requirement that the evolutionary track passes through the allowed R–$T_{\rm eff}$ region, gives a maximum mass of $2.45\ M_\odot$. If we make the sensible requirement that HZ Her is in a phase of expanding radius, to drive the mass accretion onto the neutron star, then the mass range 2.20–$2.35\ M_\odot$ is not allowed. This leaves two allowed mass ranges. For 2.15–$2.20\ M_\odot$, the track is inside the allowed region and has increasing radius just after the point of central hydrogen exhaustion. The rate of radius expansion from the stellar models is rapid, $\simeq 1 \times 10^{-3}$ cm s^{-1}, and the duration that the track inside the allowed region is very short. For 2.35–$2.45\ M_\odot$, the track is inside the allowed region with increasing radius. The rate of radius expansion is slower, $\simeq 2.5$–3.5×10^{-5} cm s^{-1}, but the duration that the track is inside the allowed region is longer (~ 1–2 Myr for 2.35 and $2.45\ M_\odot$
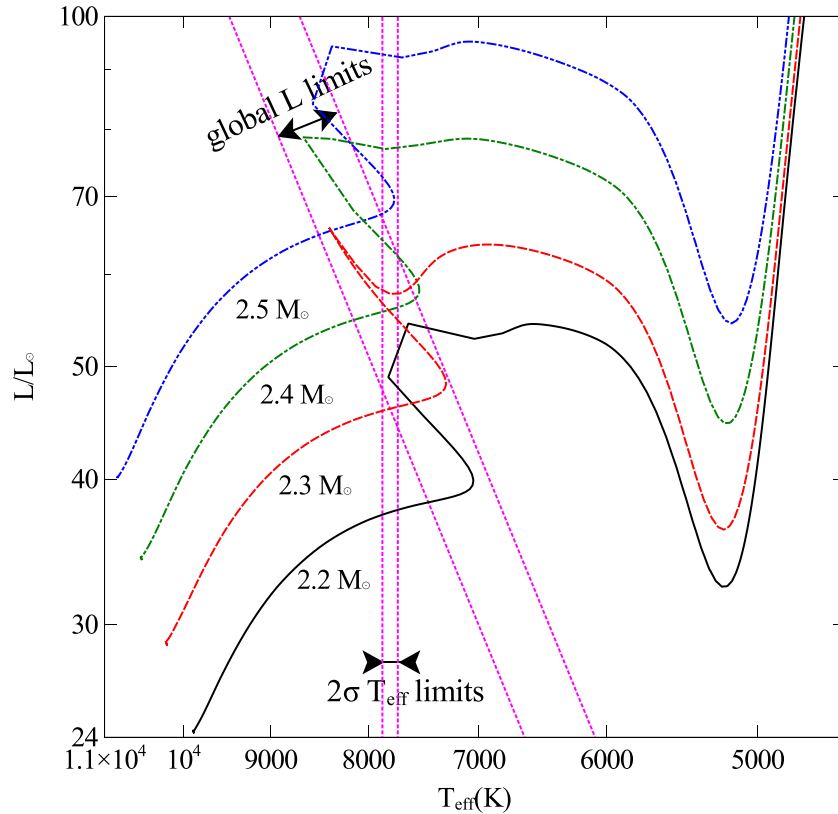
Figure 4. Stellar evolution tracks in the HR diagram for solar metallicity and initial masses (in units of $M_\odot$) of 2.2 (solid black line), 2.3 (dashed red line), 2.4 (dash-dotted green line), and 2.5 (dash-dot-dotted blue line). This range in mass covers the allowed range by the measured orbital parameters. The upper and lower 2σ limits to T_{eff} are shown by the vertical dotted lines. Upper and lower limits to luminosity based on global upper and lower limits to the radius of HZ Her are shown by the sloped dotted lines.

(A color version of this figure is available in the online journal.)

and ∼10 Myr for 2.40 $M_\odot$, where the track crosses the center of the allowed region).

We take a mass (2.40 $M_\odot$) near the center of the higher mass allowed region as an example case to illustrate the evolutionary state of HZ Her. The star enters the allowed region for HZ Her in the R–T_{eff} plane at an age of 616 Myr. It leaves the allowed region at an age of 628 Myr. Shortly thereafter, the radius continues to expand, then it decreases for a short time just before the age of 666 Myr. At this time, the radius starts to rapidly increase, while at the same time, the surface temperature changes from increasing to decreasing again. This point is marked by central H exhaustion and by the change in direction in T_{eff} (see Figure 5 for the 2.22 $M_\odot$ case). It corresponds to the sharp change in direction in the HR diagram in Figure 4 (seen as a cusp for the 2.3 and 2.4 $M_\odot$ evolutionary tracks; for 2.2 and 2.5 $M_\odot$ cases the timesteps occurred on either side of the time of central H exhaustion so the cusp was not resolved). Additionally, this point is marked by a jump in H-burning CNO cycle luminosity (from roughly 70 to 90 $L_\odot$), while the surface luminosity does not change rapidly (nearly steady at 78 $L_\odot$), rather the interior structure of the star is adjusting. He burning does not begin until 13 million years after this point in time. Between the time of central H exhaustion and time of He ignition, the central density of the core increases from ∼100 to ∼5 × 10⁴ g cm⁻³.

We note that when HZ Her enters the stage of rapid radius expansion, the mass-loss rate onto Her X-1 will increase dramatically, by a factor of ≃100. This higher mass-loss rate is super-Eddington, because the current mass transfer rate

is at about 0.1 of the Eddington rate. The likely outcome is unstable mass transfer, which happens for systems where mass transfer occurs from the more massive to less massive component, giving shrinkage of the orbit. This instability occurs on a dynamical timescale and likely yields a common envelope system (see Ivanova et al. 2013 for a recent review of common envelope systems). The common envelope system can leave behind a compact binary if the envelope is successfully ejected, consisting of the neutron star and the remaining white dwarf core of HZ Her. In this case, the white dwarf would be a He white dwarf, because He burning has not started in the core at the time of onset of the instability. The neutron star can accrete from the white dwarf, giving an LMXB system, which could subsequently evolve into a millisecond pulsar with a He white dwarf companion when the accretion ceases.

4.2.1. New Limits on Mass of Her X-1, System Inclination, and Distance

New limits on R and T_{eff} for HZ Her have been determined here. By comparing with stellar evolution calculations, two allowed narrow mass ranges are found: 2.15–2.20 $M_\odot$ if HZ Her has just passed central hydrogen exhaustion, and 2.35–2.45 $M_\odot$ if HZ Her has not yet reached central hydrogen exhaustion. Since the duration of the evolutionary track in the allowed R and T_{eff} region is about 100 times less for the lower mass range (100 kyr versus 10 Myr), the upper mass range is much more likely.
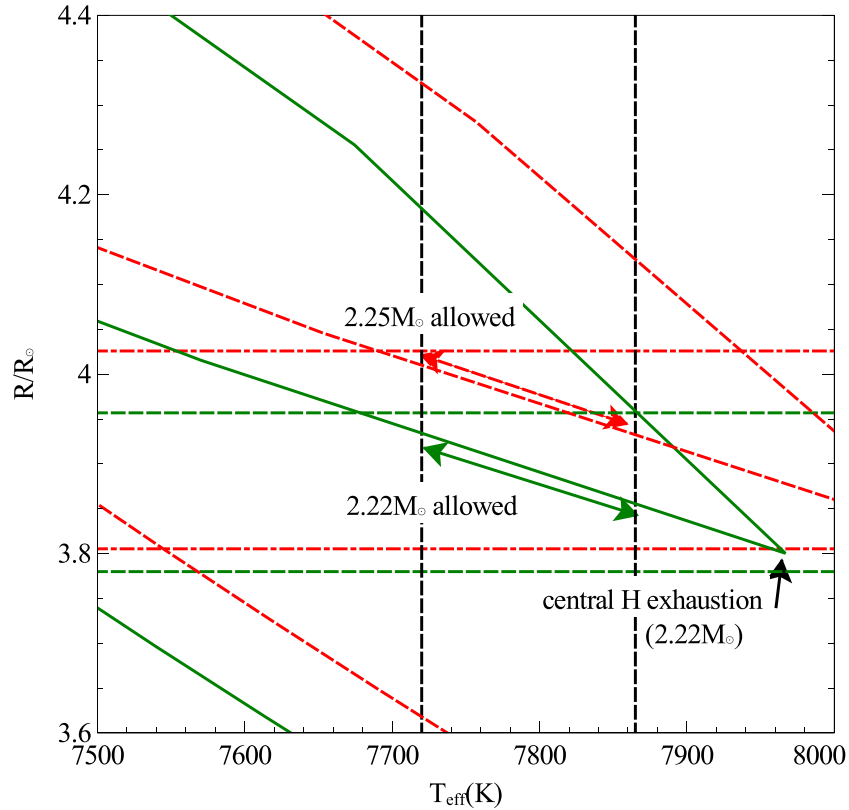
Figure 5. Evolution of 2.22 (green solid curve) and 2.25 (red dashed curve) $M_\odot$ stars of solar metallicity in the R vs. $T_{\rm eff}$ plane. The 2σ limits on $T_{\rm eff}$ from the fits to the optical spectrum of HZ Her are plotted as the vertical black dashed lines. The limits on R from the fits to X-ray eclipse are dependent on the mass of HZ Her: for 2.22 $M_\odot$, the upper and lower R limits are the horizontal green dashed lines, and for 2.25 $M_\odot$, the upper and lower R limits are the horizontal red dash-dotted lines. The 2.22 or 2.25 $M_\odot$ evolution tracks cross the 2.22 or 2.25 $M_\odot$ allowed rectangles only for segments indicated by the arrows (green, solid arrow for 2.22 $M_\odot$, red, dash arrow for 2.25$M_\odot$).

(A color version of this figure is available in the online journal.)

For either range, we can use the new limits on the mass of HZ Her, together with the information summarized in Table 9, to narrow the original range of mass of Her X-1 (M_x), system inclination, and K_c (given in Table 3). We note that the mass ratio, $q = M_x/M_c$, can be computed using the standard formula $q = K_c P_b/(2\pi a_x \sin(i))$, valid for a circular orbit, which is a good approximation here given the very small orbital eccentricity. For the lower mass range, one finds that $1.26 < M_x/M_\odot < 1.34$, $82°\!.7 < i < 90°$, and 99 km s^{-1} < K_c < 102.8 km s^{-1}. For the higher mass range, one obtains $1.47 < M_x/M_\odot < 1.71$, $80° < i < 90°$ and 105.6 km s^{-1}< K_c <119 km s^{-1}. The low-mass range for HZ Her yields a low-mass neutron star and the high-mass range yields a high-mass neutron star, but consistent with previously published estimates. However, here, Table 9 specifies the dependence of neutron star mass on inclination, K_c, and mass of HZ Her, so that an improvement in measurement of one of these quantities can yield a significant reduction in the allowed neutron star mass range.

Furthermore, with the two new allowed mass ranges for HZ Her, the distance limits (see Table 8) can be slightly improved. For the lower mass range, which has $82°\!.7 < i < 90°$ and 99 km s^{-1}< K_c < 102.8 km s^{-1}, the upper and lower distance limits are 5.73 and 6.29 kpc. For the higher mass range, which has 105.6 km s^{-1} < K_c < 119 km s^{-1}, the distance limits are 5.87 and 6.78 kpc. The uncertainties in inclination and K_c both contribute to the distance uncertainty, so that even with

the constraint on the mass of HZ Her, the distance uncertainty is large.

5. CONCLUSIONS

In this work, we analyzed X-ray eclipses of Her X-1 observed by the *RXTE*/PCA. A total of eight eclipse ingresses and egresses were found during the Main High state that were free of absorption dips. These eclipses were modeled to measure the radius of HZ Her and scale height of the atmosphere. The scale height was found to be consistent with the previous determination by Leahy & Yoshida (1995). The radius measurements are the first accurate radius measurements of HZ Her, and have small statistical uncertainty (1 part in 1000), with additional uncertainty caused by the unknown inclination and mass ratio of the HZ Her/Her X-1 binary system. The currently known orbital parameters, including an extreme range of inclinations (80°–90°) and range of K_c (radial velocity amplitude of HZ Her, equivalent to q) are summarized in Table 2. The implied semi-major axis and masses of HZ Her (M_c) and Her X-1(M_x) are given in Table 3. We found that the radii derived from all eight eclipse observations agree with each other, which confirms that we obtained a reliable measurement of radius of HZ Her. The resulting measured radius as a function of inclination and K_c is given in Table 5.

Next, we considered the constraint on HZ Her from its optical spectrum observed during mid-eclipse, when we see only the

unheated face of HZ Her. We fitted the spectrum with Kurucz model atmospheres for a range of $T_{\rm eff}$ and metallicity with the surface gravity determined by the allowed masses (from orbital parameters) and allowed radii (from X-ray eclipse). We determined a 2σ allowed range in $T_{\rm eff}$ of 7720 K–7865 K, and in metallicity of $\log(Z/Z_\odot) = -0.27$ to $+0.03$. With the observed continuum flux from HZ Her during mid-eclipse, we used the model surface flux and its 2σ ranges to determine a best-fit distance to HZ Her and 2σ upper and lower limits. Because the radius inferred from eclipse depends on inclination and K_c, the results are presented in Table 8 as a function of inclination and K_c. The best-fit distance is 6.10 kpc, and the overall upper and lower limits are 5.73 kpc and 6.98 kpc at the extremes of allowed inclination and K_c.

Next, we computed stellar evolutionary tracks for stars of various mass and solar metallicity consistent with the narrow metallicity range from the spectral fits. We required consistency of the model stars with both the temperature, $T_{\rm eff}$, and radius of HZ Her, which has not been done before. The radius derived from X-ray eclipse depends on inclination and K_c, thus each model mass has a different constraint on radius. We calculated the constraints separately for each model mass. Only stars with mass in one of two ranges of (2.15–2.20 $M_\odot$ and 2.35–2.45 $M_\odot$) agree with the $T_{\rm eff}$ and radius constraints at some point in their stellar evolution. Model stars in the low-mass range are just past the time of central hydrogen exhaustion in their evolution. Model stars in the higher mass range are not much younger than the time of central hydrogen exhaustion. For the low-mass range, the star is just entering the phase of rapid radius expansion, which should lead to rapid, unstable mass transfer. For the higher mass range, the star will enter this phase in about 40 Myr from now. At the time of rapid radius expansion, HZ Her/Her X-1 will likely become a common envelope system, and then may emerge as an LMXB (neutron star with He white dwarf companion).

With the new mass limits on HZ Her from the stellar evolution calculations the range of allowed mass of the neutron star was determined. For the lower mass range, the neutron star is low mass ($\simeq 1.34$ $M_\odot$), while for the higher mass range, the neutron star is high mass ($\simeq 1.5$–1.7 $M_\odot$). Improvement in measurement of K_c or system inclination can lead to significant improvement in the limits on distance to Her X-1 and on neutron star mass.

REFERENCES

Anderson, S. F., Wachter, S., Margon, B., et al. 1994, ApJ, 436, 319
Boroson, B., Blair, W. P., Davidsen, A. F., et al. 1997, ApJ, 491, 903
Cheng, F. H., Vrtilek, S. D., & Raymond, J. C. 1995, ApJ, 452, 825
Choi, C., Dotani, T., Nagase, F., et al. 1994, ApJ, 427, 400
Choi, C., Seon, K., Dotani, T., & Nagase, F. 1997, ApJL, 476, L81
Crosa, L., & Boynton, P. E. 1980, ApJ, 235, 999
Dal Fiume, D., Orlandini, M., Cusumano, G., et al. 1998, A&A, 329, L41
Deeter, J., Crosa, L., Gerend, D., & Boynton, P. 1976, ApJ, 206, 861
Eggleton, P. P. 1971, MNRAS, 151, 351
Eggleton, P. P. 1983, ApJ, 268, 368
Gerend, D., & Boynton, P. 1976, ApJ, 209, 652
Igna, C. D. 2010, PhD Thesis, Univ. of Calgary
Igna, C. D., & Leahy, D. A. 2011, MNRAS, 418, 2283
Igna, C. D., & Leahy, D. A. 2012, MNRAS, 425, 8
Ivanova, N., Justham, S., Chen, X., et al. 2013, A&ARv, 21, 59
Ji, L., Schulz, N., Nowak, M., Marshall, H. L., & Kallman, T. 2009, ApJ, 700, 977
Jimenez-Garate, M. A., Raymond, J. C., Liedahl, D. A., & Hailey, C. J. 2005, ApJ, 625, 931
Klochkov, D., Staubert, R., Postnov, K., Shakura, N., & Santangelo, A. 2009, A&A, 506, 1261
Kurucz, R. L. 1993, IAU Colloq. 138: Peculiar versus Normal Phenomena in A-type and Related Stars, ed. M. M. Dworetsky, F. Castelli, & R. Faraggiana (San Francisco, CA: ASP), 87
Leahy, D. A. 1995a, ApJ, 450, 339
Leahy, D. A. 1995b, A&ASS, 113, 21
Leahy, D. A. 1997, MNRAS, 287, 622
Leahy, D. A. 2002, MNRAS, 334, 847
Leahy, D. A. 2003, MNRAS, 342, 446
Leahy, D. A. 2004a, MNRAS, 348, 932
Leahy, D. A. 2004b, ApJ, 613, 517
Leahy, D. A., & Igna, C. 2010, ApJ, 713, 318
Leahy, D. A., & Igna, C. 2011, ApJ, 736, 74
Leahy, D., & Scott, D. M. 1998, ApJL, 503, L63
Leahy, D. A., & Yoshida, A. 1995, MNRAS, 276, 607
McCray, R., Shull, M., Boynton, P., et al. 1982, ApJ, 262, 301
Oke, J. B. 1976, ApJ, 209, 547
Oosterbroek, T., Parmar, A., Martin, D., & Lammers, U. 1998, A&A, 329, L41
Oosterbroek, T., Parmar, A. N., Dal Fiume, D., et al. 2000, A&A, 353, 575
Reynolds, A., Quaintrell, H., Still, M., et al. 1997, MNRAS, 288, 43
Scott, D. M., & Leahy, D. 1999, ApJ, 510, 974
Scott, D. M., Leahy, D. A., & Wilson, R. B. 2000, ApJ, 539, 392
Shakura, N., Postnov, K., & Prokhorov, M. 1998, A&A, 331, L37
Shulman, S., Friedman, H., Fritz, G., Henry, R. C., & Yentis, D. J. 1975, ApJL, 199, L101
Staubert, R., Klochkov, D., & Wilms, J. 2009, A&A, 500, 883
Still, M., Quaintrell, H., Roche, P., & Reynolds, A. 1997, MNRAS, 292, 52
Voloshina, I., Lyutyi, V., & Sheffer, K. 1990, SvAL, 16, 257
Vrtilek, S. D., & Cheng, F. H. 1996, ApJ, 465, 915